Journal of Solid State Chemistry 183 (2010) 2886–2894

Contents lists available at ScienceDirect

Journal of Solid State Chemistry

journal homepage: www.elsevier.com/locate/jssc

Investigation of structural, morphological, luminescent and thermal properties of combusted aluminium-based iron oxide

S.S. Shinde, K.Y. Rajpure *

Electrochemical Materials Laboratory, Department of Physics, Shivaji University, Kolhapur 416004, India

ARTICLE INFO

Article history:
Received 20 June 2010
Received in revised form
16 September 2010
Accepted 27 September 2010
Available online 1 October 2010

Keywords:
Combustion
Iron oxide
Morphology
XPS
PL
Thermal conductivity
Complex impedance

ABSTRACT

Nanocomposites of aluminium integrated hematite α-Fe_2O_3 are synthesized by combustion route using aqueous solutions of AR grade ferric trichloride and aluminium nitrate as precursors. The influence of aluminium incorporation on to the morphology, XPS, photoluminescence and thermal properties has been investigated. The FESEM and AFM micrographs depict that the samples are compact and have homogeneously distributed grains of varying sizes ($\sim$20–60 nm). Chemical composition and valence states of constituent elements in hematite are analyzed by XPS. In room temperature photoluminescence (PL) study, we observed strong violet emission around 436 nm without any deep-level emission and a small PL FWHM indicating that the concentrations of defects are responsible for deep-level emissions. The specific heat and thermal conductivity study shows the phonon conduction behavior is dominant. We studied interparticle interactions using complex impedance spectroscopy. We report a new potential candidate for its possible applications in optoelectronics and magnetic devices.

1. Introduction

The synthesis of nanocomposites comprising nanoscale materials with different physico-chemical properties has been investigated widely in efforts to design advanced materials with enhanced properties [1]. During last decade a large number of investigations have been focused on iron oxide based nanoparticles for their potential applications in ferrofluids [2], magnetocaloric refrigeration [3] and biotechnology. Besides, these materials offer several potential biomedical applications, specifically, for magnetically controlled drug delivery [4], magnetic resonance imaging [5], tissue repair, immunoassay, detoxification of biological fluids [6] and as nanosensors [7]. Recent interest in this area has led to colloidal iron oxide particles for their better usage in biomedicine [8]. By selecting appropriate constituent elements, the associated crystals and derived electronic structures of oxides can be altered by manipulating the delicate equilibrium in the bonding requirements of a lattice, thus leading to a wide spectrum of physical properties. Their functionalization with Al has demonstrated vast potential in catalysis [9] and biotechnological applications, namely protein separation [10], cancer diagnosis [11], as biosensors and bioactuators [12]. In most of the biological applications, magnetic properties of these particles, and in particular superparamagnetism, have been considered to contribute significantly [13]. The incorporation of metal/metal ions into iron oxide(s) also results in the formation of 'delafossites' [9]. These materials have found utility in electric switch contacts, soldering, increasing high-density storage capacity [14], thermoelectric devices [15,16], field emission displays (FEDs) [17], ozone sensors [18], photocatalytic hydrogen generators [19], magnetic semiconductors for spintronics [20] and optoelectronic technology [21,22]. In the literature we did not come across any report on the synthesis of aluminium-based iron oxide.

The present work reports a new method for the synthesis of nano-sized aluminium iron oxide nanocomposite with a narrow size distribution by interacting colloidal α-Fe_2O_3 with aluminium particles. The resulting composite system has been characterized by using XRD, FESEM, AFM, XPS, PL, impedance and hysteresis techniques. Thermal measurements were performed for the study of specific heat and thermal conductivity under different experimental conditions. Also we have studied an interparticle interactions using complex impedance spectroscopy.

2. Experimental

The aluminium-added iron oxide samples were prepared by a combustion route using AR grade equimolar (0.1 M) ferric trichloride ($FeCl_3$) and aluminium nitrate ($Al(NO_3)_2$ of s. d. fine Ltd, Mumbai, with 98.6% and 99.5% purity. The preparation conditions

* Corresponding author. Fax: +91 231 2691533.
E-mail address: rajpure@yahoo.com (K.Y. Rajpure).

0022-4596/$ - see front matter © 2010 Elsevier Inc. All rights reserved.
doi:10.1016/j.jssc.2010.09.035

were carefully controlled. A mixture of precursors in atomic proportion was taken in to a Pyrex dish and melted by heating at 80 °C. Then appropriate amount of fuel glycine was added in the mixture. After evaporation of the water content, the mixture ignited to combust with a flame, giving voluminous and foamy samples. The aluminium doping (in starting solution) was varied from 0 to 20 at%. The synthesized powder was annealed at 350 °C. These compositions were further mixed with polyvinyl alcohol as a binder and pressed into pellets of 15 mm diameter and 2–3 mm thickness using a hydraulic press (5 ton for 5 min). Then prepared pellets were annealed for 400 °C for 1 h for the removal of binder.

The morphological characterization of the samples was studied by using field emission scanning electron microscopy (FESEM, Model: JSM-6701 F, Japan). The surface topography of samples was further analyzed from AFM images taken by means of the atomic force microscopy (AFM, Digital Instrument, Nanoscope III) operated at room temperature. AFM images were collected in contact mode on a molecular imaging system using a silicon nitride cantilever. The chemical composition and valence states of constituent elements were analyzed by using X-ray photoelectron spectroscopy (XPS, Physical Electronics PHI 5400, USA) with monochromatic Mg–$K\alpha$ (1253.6 eV) radiation source. Photoluminescence (PL) spectra were obtained using a closed-cycle liquid helium cryogenerator (APD, SH-4, USA), a spectrometer (f=0.5 m, Acton Research Co., Spectrograph 500i, USA) and intensified photodiode array detector (Princeton Instrument co., IRY1024, USA). All spectra were measured at room temperature with an Ar^+ ion laser as a light source using an excitation wavelength of 325 nm. The specific heat capacity and thermal conductivity was measured by C-T meter made by Teleph Pvt. Ltd., France. The impedance parameters namely Z' and Z'' for all the samples were measured at various temperatures in the frequency range 20 Hz–1 MHz using a precision LCR meter bridge (model HP 4284 A). Magnetic properties were studied using hysteresis loop tracer (Magneta B–H loops tracer) at a maximum applied field of 4 KOe.

3. Results and discussion

3.1. Structural analysis

Fig. 1 shows X-ray diffraction patterns of the undoped and typical 10 at% Al added iron oxide samples. From these patterns, it is seen that synthesized samples are of hematite (α-Fe_2O_3) phase. The samples are polycrystalline and fit well with the rhombohedral crystal structure having space group $R3$ (148). These samples of α-Fe_2O_3 are in correspondence with 03-0800 in Powder Diffraction File (PDF) collected by the Joint Committee on Powder Diffraction Standards (JCPDS). For the 10 at% Al:Fe_2O_3 sample, the diffraction angle of the (202) peak is almost in agreement with the Fe_2O_3 bulk single crystal, implying that no evident residual stress or inclusion-induced lattice distortion has developed in the Fe_2O_3 sample due to Al incorporation [23,24]. Some weak reflections such as (012), (104), (110), (006), (113), (202), (024) and (116) have also been observed but with small intensities. After addition of aluminium into the host lattice, intensity of all reflections goes on decreasing.

The average crystallite size is calculated employing Scherrer's equation

$$D = \frac{0.9\lambda}{\beta \cos\theta} \quad (1)$$

where D is the crystallite size, λ is wavelength of X-ray, β is full width at half maximum in radian, and θ is Bragg's angle. The average crystallite size is of the order of 18 and 12 nm for undoped and 10 at% aluminium added samples, respectively.

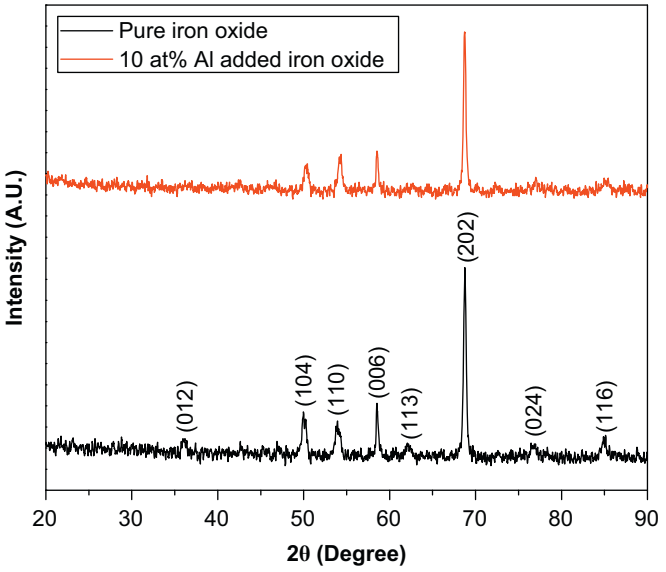

Fig. 1. X-ray diffraction patterns of undoped and typical 10 at% Al-added iron oxide samples

3.2. Surface morphological study

Fig. 2(a)–(e) shows the FESEM images of aluminium added (0–20 at% doping concentration) iron oxide samples. The micrographs depict that the samples are compact and homogeneous distribution of grains with varying sizes have been observed. The pure iron oxide sample shows the agglomerated highly dense, compact and homogeneous structure. The large value of the grain size observed by SEM may be explained by the tendency of the small grains to aggregate to the big grains in the sample. Apparently, the Al-doping affects the grain size leading to a grain width reduction, as clearly observed in Fig. 2(b)–(e). As the doping concentration increases from 0 to 10 at%, compactness of grains and grain size decreases and number of grains increases. From the images, it is confirmed that the powder samples are converting from the microcrystalline to nanocrystalline phase. Average grain size observed for the all samples are in the range 15–55 nm. Therefore, it can be concluded that the morphology and grain size affects due to doping concentration. There are two possibilities associated with the phenomena. One is the effect from outside and the other from inside. It is known that, the oxygen and vapor in the air would have big effect on the morphology. When there is an exchange of oxygen between grains and air, the collapse may happen. We tend to agree with the second mechanism that the collapse is probably due to the strain release of crystallites due to high temperature. The formation of 3D crystallites is mainly governed by surface energy, elastic strain and surface diffusion kinetics. Theoretically, small regions of high strain will evolve as grooves or pits if, strain is not homogeneously relieved during the growth [25]. Therefore, we can assume that the uneven component distribution of Fe_2O_3 grow at relatively low concentrations could result in local sites with high strain. As a result, the depositing materials diffused away from these high-strain sites.

Fig. 3(a,b) shows two- and three-dimensional atomic force microscopy (AFM) images of pure and optimized 10 at% aluminium added iron oxide powder samples. The images were recorded on $1 \times 1\ \mu m^2$ planar in contact mode at the scan rate of 10.17 Hz. Uniformly distributed agglomerated grains of varying sizes are seen. It is seen that grain size decreases after incorporation of aluminium. One can see that by increasing the number of thermal treatments grains of regular shapes develop

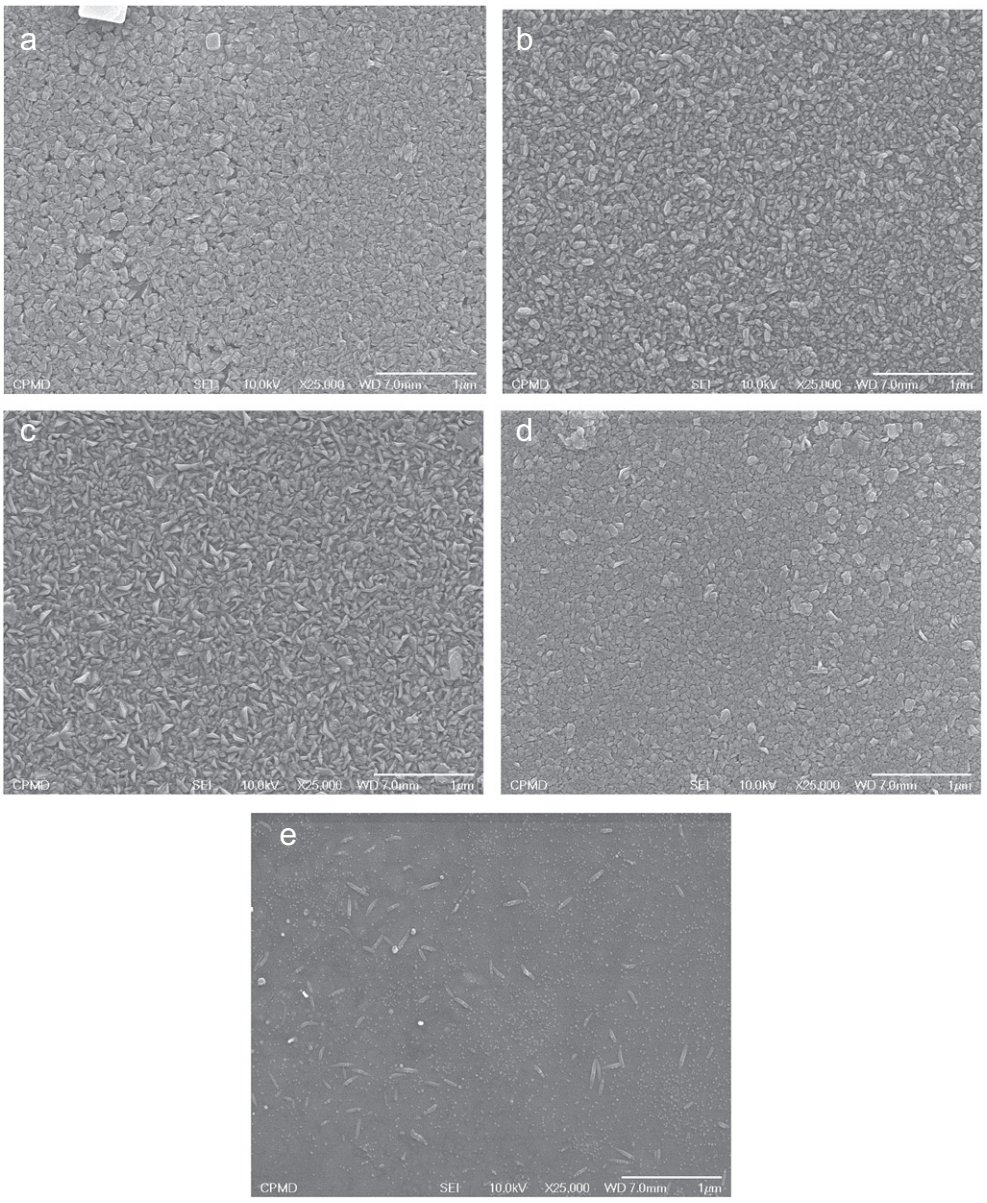

Fig. 2. FE-SEM images of (a) pure Fe_2O_3, (b) 5 at%, (c) 10 at%, (d) 15 at% and (e) 20 at% Al:Fe_2O_3 samples.

on to the surface indicating a significant degree of surface order on the scale of several micrometers. The apparent dimension of these grains is in the region of 100 nm. This shows that the samples are crystallized and moreover that there is a preferred orientation of these regularly shaped grains, which suggests the growth of a microcrystalline sample.

3.3. X-ray photoelectron spectroscopy

The chemical composition and valence states of constituent elements in hematite α-Fe_2O_3 are analyzed by the X-ray photoelectron spectroscopy. Fig. 4(a) shows the XPS spectrum of O 1*s* core-level of pure and typical 10 at% aluminium added iron oxide samples. The binding energy of O 1*s* photoelectrons exhibited a broad peak, which can be splitted into three contributory phases ~530, 531.7 and 532.3 eV. In addition to the peak originating from the Fe_2O_3 lattice oxygen (530.0 eV), the peak at 531.7 eV can be attributed to the oxygen of the –OH species in α-FeOOH or chemical bonded –OH group at the surface of α-Fe_2O_3 [26], while at 532.3 eV should be from the oxygen in SO_4^{2-} [27]. It is seen that the Fe_2O_3 lattice oxygen state is dominant in the pure iron oxide sample, but in case of Al added sample it shows two peaks for 529.96 and 531.79 eV. Due to Al incorporation the dominance of 529.96 eV peak decreases. Mostly the O 1*s* peak has been seen in the measured binding energy region of 529–535 eV and for chemisorbed oxygen on the metal surface, binding energy is obtained in the region 530–530.9 eV, therefore, the low binding energy component centered at 530.0 eV of the O 1*s* spectrum is attributed to chemisorbed oxygen (O^{2-} ions) [28]. The high binding energy components located at 531.7 and 532.3 eV are probably attributed to the presence of loosely bound oxygen on the surface of iron oxide sample belonging to a specific species, e.g.,carbon trioxide (–CO_3), or corresponds to hydroxides. [29,30].

Fig. 4(b) shows the Fe 2*p* core level XPS spectrum as a function of binding energy for pure and 10 at% Al added Fe_2O_3 powder sample. Due to spin–orbit coupling, the Fe 2*p* core level splits into $2p_{1/2}$ and $2p_{3/2}$ components. From figure, there are two obvious peaks located at ~711 and ~724 eV due to Fe^{3+} and Fe^{2+} ions, respectively, and a satellite peak at ~719 eV, which is

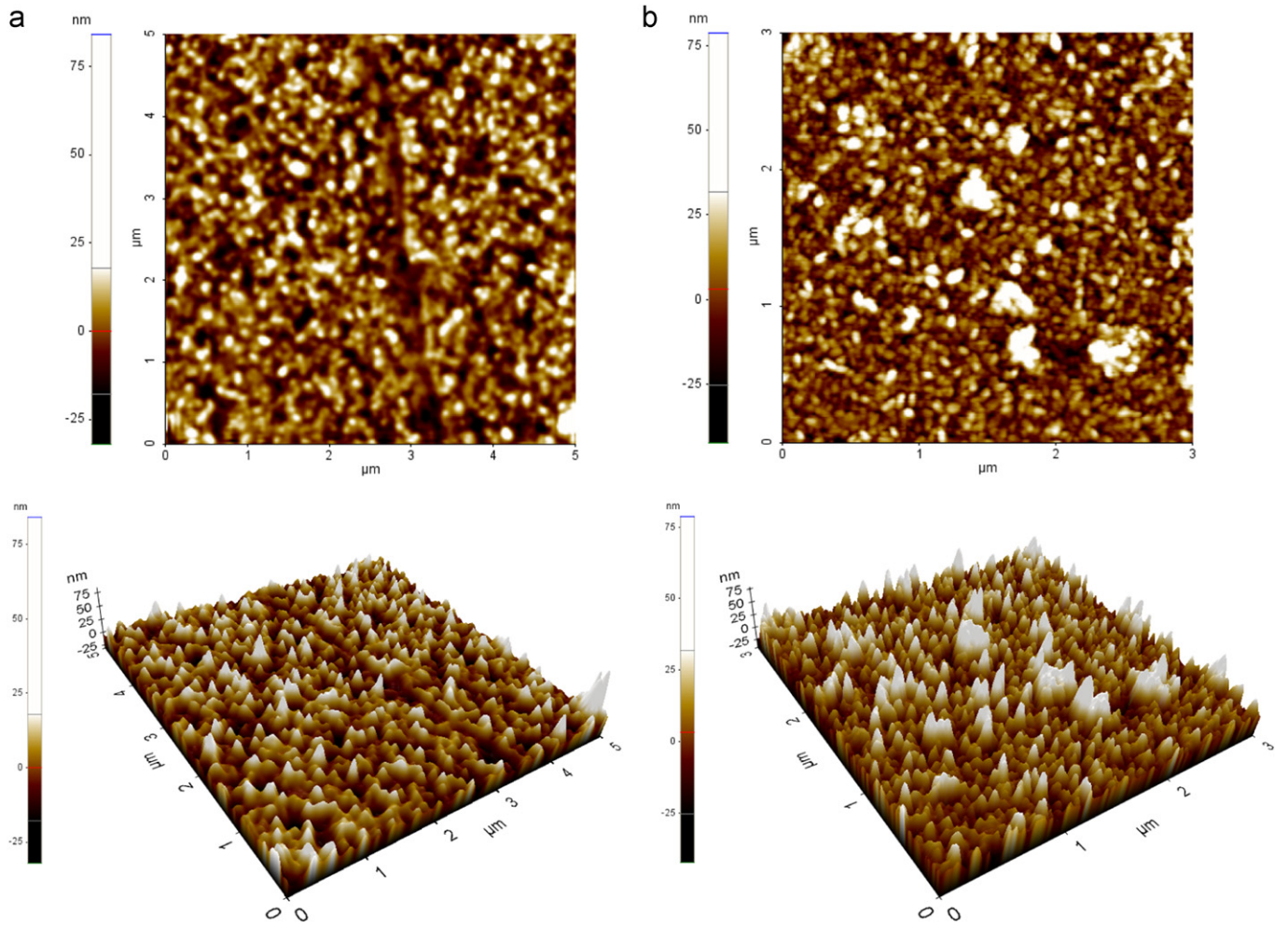

Fig. 3. AFM images of (a) pure Fe_2O_3 and (b) 10 at% Al-added iron oxide powder samples with 1×1 μm^2 planar.

characteristic of ferric oxides. The intensity of these core levels decreases due to Al incorporation. The observed broadening of the Fe $2p_{1/2}$ and $2p_{3/2}$ peaks at 10 at% aluminium doping is 13.68 eV indicating the existence of Fe^{2+}. The presence of a satellite peak situated at ~719 eV, which is characteristic of Fe^{3+} in γ-Fe_2O_3, suggests that γ-Fe_2O_3 exists in the film. It has been confirmed that a decrease in the coordination numbers of ferric cations located at the surface provides some effect on the binding energy. The Al 2*p* region of the deposited film is shown in Fig. 4(c). The less proportion of aluminium is observed as compared to bulk incorporated aluminium. The peaks of Al $2p_{3/2}$ and Al $2p_{1/2}$ locate around 74 and 79 eV indicating that the Al element mostly exists in the valence of +3.

3.4. Photoluminescence study

Fig. 5 shows the room temperature PL spectra of the pure and aluminium added iron oxide powder samples measured in the wavelength range 300–850 nm. A strong PL violet emission is observed at 436 nm. Violet emission is probably due to radiative defects related to the interface traps existing at the grain boundaries and emitted from the radiative transition between these levels and valence band. As the doping concentration of aluminium increases, PL peak intensity increases (becomes sharper) up to 10 at% Al and then decreases (becomes broader). The PL full width at half maximum (FWHM) is decreased from pure to 10 at% Al-added iron oxide (185–92 nm) and then increases for higher doping concentrations. The iron oxide displays three major PL peaks as mentioned earlier: an UV near-band-edge emission peak around 420–436 nm, a blue emission around 464 nm and a red emission around 700 nm. It is generally accepted that the violet and red emissions are associated with oxygen vacancies and interstitial Fe ions in the Fe_2O_3 lattice. In contrast, our pure iron oxide sample displayed only violet emission peaks around 430–440 nm and no observable deep-level emissions. Excitation peak (464 nm) is shifted from pure to added iron oxide samples by 16 nm. The shift of the exciton peak with particle size is probably due to a quantum-confinement induced energy gap enhancement. The thermal energy at room temperature can break the bound excitons into free excitons, because of the small binding energy of bound excitons. The shoulder PL peak at 420 nm can be associated with oxygen vacancy and the donor–acceptor band transition resulting from Al doping and the transition from excited level to based level. However, it may be attributable to recombination of deep trapped charges and photogenerated electrons from the conduction band on account of an increase in oxygen vacancies. The other weak emission about 700 nm has been attributed to the radiative recombination of electrons trapped at oxygen vacancy related states near the conduction band edge with holes in deep Fe-related surface states. These samples are might be useful in luminescence technology.

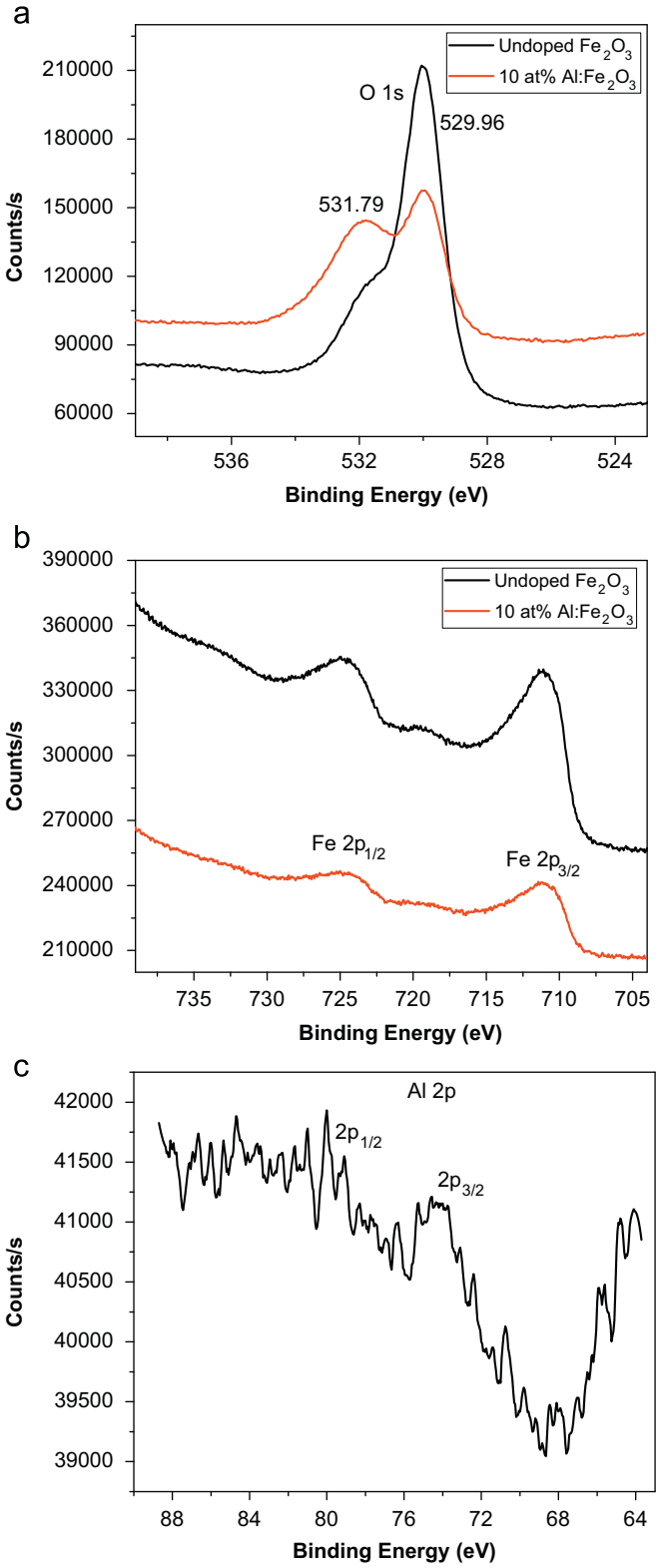

Fig. 4. Narrow scan XPS spectra of (a) O 1 s core level, (b) Fe 2*p* region ($2p_{3/2}$ and $2p_{1/2}$) and (c) Al 2*p* core level region for of unadded and typical 10 at% Al-added iron oxide samples, respectively.

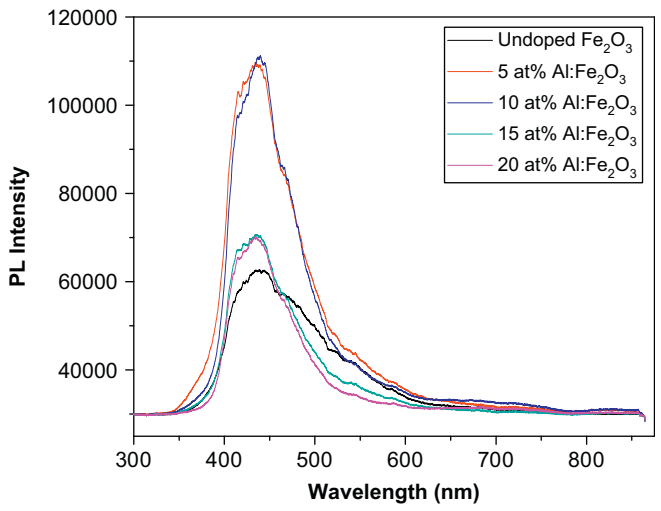

Fig. 5. Photoluminescence spectra of aluminium added iron oxide samples as a function of doping concentration.

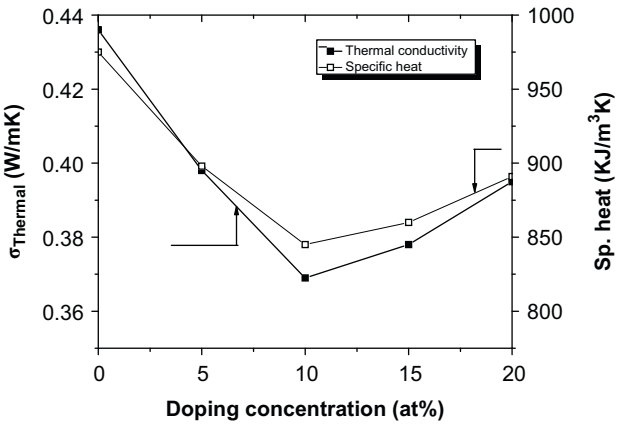

Fig. 6. Variation of specific heat and thermal conductivity against aluminium doping concentration.

3.5. Thermal conductivity

It is essential to understand the thermo-physical properties of the iron oxide powder, when working on those industrial and scientific applications that involve not only equipment design but also analysis, modeling and process control, where there are temperature dependent physical, chemical and biochemical changes. Thermal conductivity analysis is done with the help of the following relation:

$$\Delta T = \frac{RI^2}{L}\frac{1}{4\pi k}\left[\ln(t)+C\right] \quad (1)$$

where R is the resistance of the ring probe, k the thermal conductivity, I the current, t the pulse time, L the length of ring probe and C the integration constant. The variation of specific heat and thermal conductivity with respect to the doping concentration is illustrated in Fig. 6. Specific heat and thermal conductivity decreases up to 10 at% Al doping concentration (attains minimum value 845 KJ/m^{3}K and 0.369 W/mK, respectively) and further increases for higher concentrations. The decrease in thermal conductivity means that a phonon conduction behavior is dominant in these polycrystalline powder samples [31], while the increase in thermal conductivity for higher concentrations is mainly attributed to the significant change in microstructure. Apart from the contribution of the microstructure, the lower thermal conductivity of samples can be attributed to the intrinsic factors. The thermal conductivity for a crystalline solid is due to changes of lattice vibrations, which are usually described in terms of phonons. In phonon conduction, the mean free path is lowered when defect concentration is increased. This implies that the Al

addition tends to increase the defect concentration. The boundaries between grains and grain layers near the surface always contain a large number of impurity atoms and broken bonds [32] which deform the lattice and excite the surrounding phonon scattering fields of elastic stresses. In view of the smallness of the grain size, the concentration of these defects in pressed samples is significantly higher than the prepared from vapor phase, which causes a lower thermal conductivity in the sample.

The expression of the thermal conductivity is derived by Debye described as [33]

$$k = \frac{1}{3} t_p C_v v_m \tag{2}$$

where C_v is the specific heat, v_m the phonon velocity and t_p the mean free path for scattering of phonons. The actual values of thermal conductivity depend sensitively on the defects such as vacancies and solutes which are strong phonon scatterers influencing t_p.

The effect of point defects on the phonon mean free path t_p is given by Klemens [34] as follows:

$$\frac{1}{t_p} = \frac{\alpha^3}{4\pi v^4} \omega^4 c \left(\frac{\Delta M}{M}\right)^2 \tag{3}$$

where α^3 is the volume per atom, v the transverse wave speed, ω the phonon frequency, c the defect concentration per atom, M the average mass of the host atom, $M+\Delta M$ the average mass of the solute atom, and for vacancies, the value of $\Delta M/M$ is calculated by

$$\frac{\Delta M}{M} = \frac{M_\alpha}{2} - 2 \tag{4}$$

where M is the average mass per atom, M_α the mass of the missing atom, and the term -2 accounts for the potential energy of the missing linkages, or twice the potential energy per atom.

3.6. Complex impedance spectroscopy

The complex impedance (Z) can be represented as $Z^* = Z' - iZ'' = |Z|\cos\theta - i|Z|\sin\theta$, where Z' and Z'' are the real and imaginary parts of complex impedance, and $|Z|$ and θ are the modulus and complex angle of the complex impedance, respectively. The complex impedance formalism helps in determining interparticle interactions like grains, grain boundary effects, etc. Due to the polycrystalline nature of Fe_2O_3, the barrier is modeled as double layer over the grains region. The resistance contributions are generally represented by three parallel circuits (R–C) connected in series and corresponding to the bulk, the grain boundary and the diffusion. Fig. 7(a,b) represents the real (Z_r) and imaginary component (Z_i) in the complex plan for pure iron oxide and typical 10 at% Al-added iron oxide samples at 50–200 °C temperature. The center of the semicircle is localized below the real axis ascribed to a constant phase element, a single barrier of the junction Fe_2O_3/electrolyte confirming relaxation time. The impedance spectrum is characterized by the appearance of semicircle arcs whose pattern changes, but not its shape, when the temperature is increased. Such pattern tells us about the electrical process occurring within the sample and their correlation with the sample microstructure, when modeled in terms of an electrical equivalent circuit [35]. The equivalent circuit configuration for the impedance plane plot is $R_g+R_{gb}||C_{gb}$ shown in Fig. 7(c). The intersect with real axis of the semicircle at low frequencies is ascribed to the total resistance RT. On the other hand, the impedance response of grain dominates at high frequencies and the resistances of grain R_g can be deduced from the left intersect of the semicircle with real axis. The intercept of the semicircle with the real axis (Z′) at low frequency represents the sum of the resistance of grains and grain boundaries, while the intercept at high frequency represents the resistance of the grains only. Grain boundary resistance decreases with rise in temperature, it seems to be due to the fact that the grain boundary effect has assisted in lowering the barrier to the motion of charge carriers paving the way for increased electrical transport with rise in temperature. The evidences of grain boundary conduction have been observed in perovskite ceramic, ceramic conductors and also in ceramic dispersed ionically conducting composite polymers. The expression of real (Z') and imaginary (Z'') components of impedance related to the equivalent circuit are

$$Z' = R_g + \left(\frac{R_{gb}}{1 + R_{gb}^2 C_{gb}^2 \omega^2}\right) \tag{5}$$

$$Z'' = \frac{R_{gb}^2 C_{gb} \omega}{1 + R_{gb}^2 C_{gb}^2 \omega^2} \tag{6}$$

where $\omega = 2\pi f$ and f the frequency, R_g and C_g are the resistance and capacitance of the grain while R_{gb} and C_{gb} are that of grain boundary. Depending upon the relative rate of decrease of R_g and R_{gb}, and at the same time the relative rate of increase of C_g and C_{gb}, with ω as the variable, the complex impedance curves gradually and successively change from one shape to the other [36], at different temperatures. The impedance value is typically higher at lower temperatures in the low-frequency region and decreases gradually with increasing frequency. Also, Z' decreases with increasing temperature indicating an increase in ac conductivity. The value of Z' appears to merge in the high-frequency region irrespective of temperature; this result may possibly be related to the release of space charge as a result of reduction in the barrier properties of material with rise in temperature, and may be a responsible factor for the enhancement in conductance of the material with temperature at high frequencies. The values of Z' for all temperatures merge at higher frequencies can be interpreted by the presence of space charge polarization. This interpretation was confirmed by the higher impedance values at lower frequencies.

The frequency-dependent variation of the imaginary part of impedance (Z″) at different temperatures of pure and 10 at% Al-added iron oxide sample is shown in Fig. 8(a,b). The intensity of imaginary peaks decreases with aluminium doping as compared to pure iron oxide sample. Figure shows, as temperature increases peak intensity decreases and the peak position shifts towards low frequency; the Z″ values for all temperatures merge above 30 kHz. The curves show that Z″ exhibits the maximum value for given temperature of measurement at a particular frequency (Z''_{max}) and then decreases continuously with further increase in frequency and temperature indicating single relaxation process in the system. The frequency of the maximum, shifts toward lower values with temperature, indicating decrease in loss. The variation of the real part of impedance (Z′) with frequency at different temperatures of pure and 10 at% Al-added iron oxide sample is shown in Fig. 8(c,d). The intensity of real peaks decreases with aluminium doping in the sample. Similar to that of Z'', the magnitude of Z' also decreases with an increase in temperature and frequency (beyond the peak frequency), and all the curves coincide for the frequency above 2 kHz. This may be due to the release of space charges. The observed presence of a single peak suggests single relaxation process and indicates an increase in ac conductivity with temperature and frequency.

3.7. Magnetic properties

Fig. 9 depicts the B–H hysteresis loops of pure and Al added iron oxide samples. All samples exhibit magnetic behavior

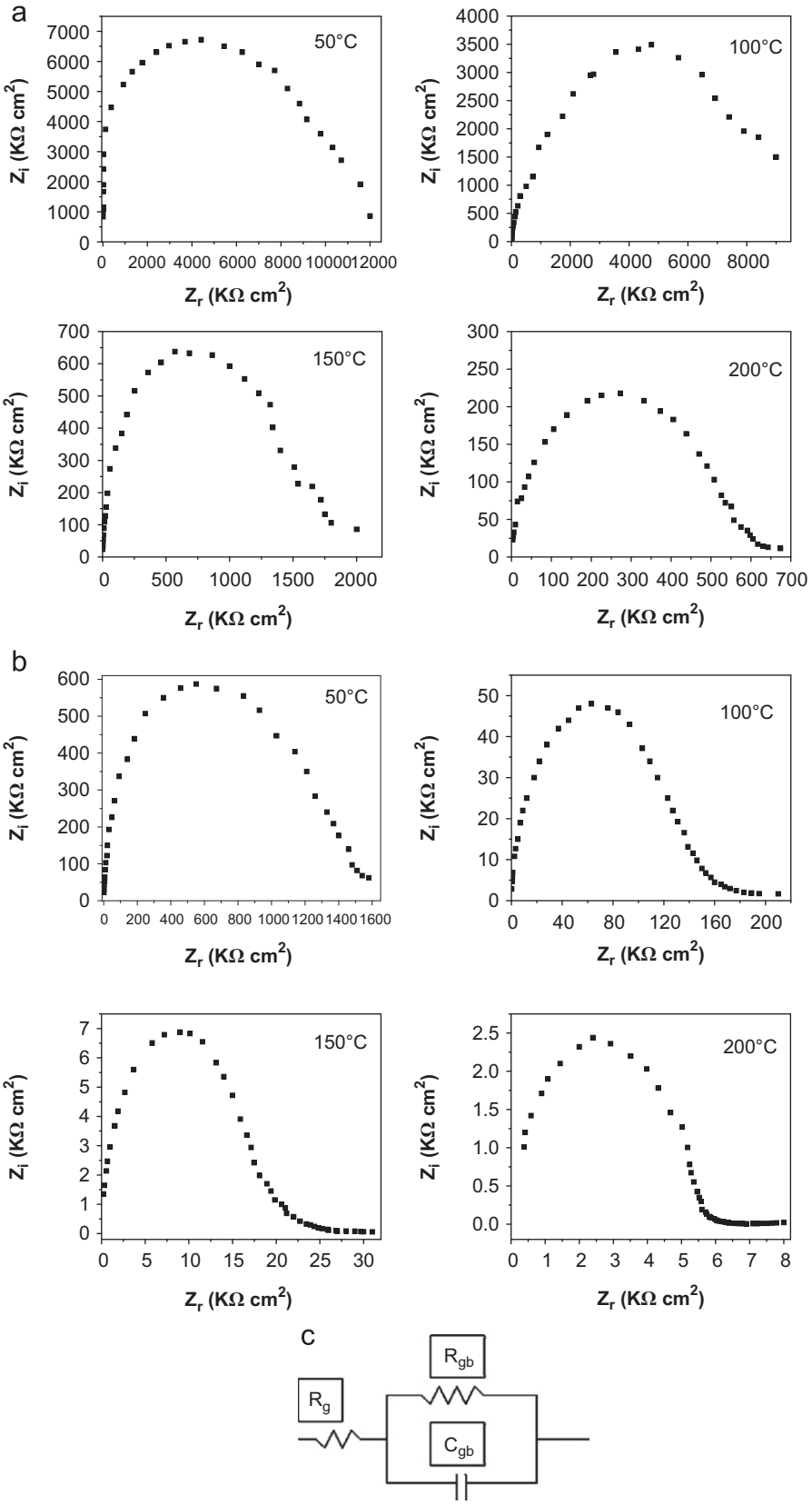

Fig. 7. Complex impedance spectra of (a) pure iron oxide, (b) typical 10 at% Al-added iron oxide samples at various temperatures (50–200 °C) and (c) equivalent circuit diagram.

indicating presence of an ordered magnetic structure in the iron oxide samples at room temperature. All samples show saturation magnetization (M_s) above magnetic field strength of ~2 kOe. M_s increases from 16.17 to 45.76 emu/gm with Al percentage. With substitution of Al^{3+}, the saturation magnetization (M_s) increases. Since the compositions were planned to get high values of saturation magnetization, the increase in M_s can be understood as a consequence of distribution of aluminium ions in preferred

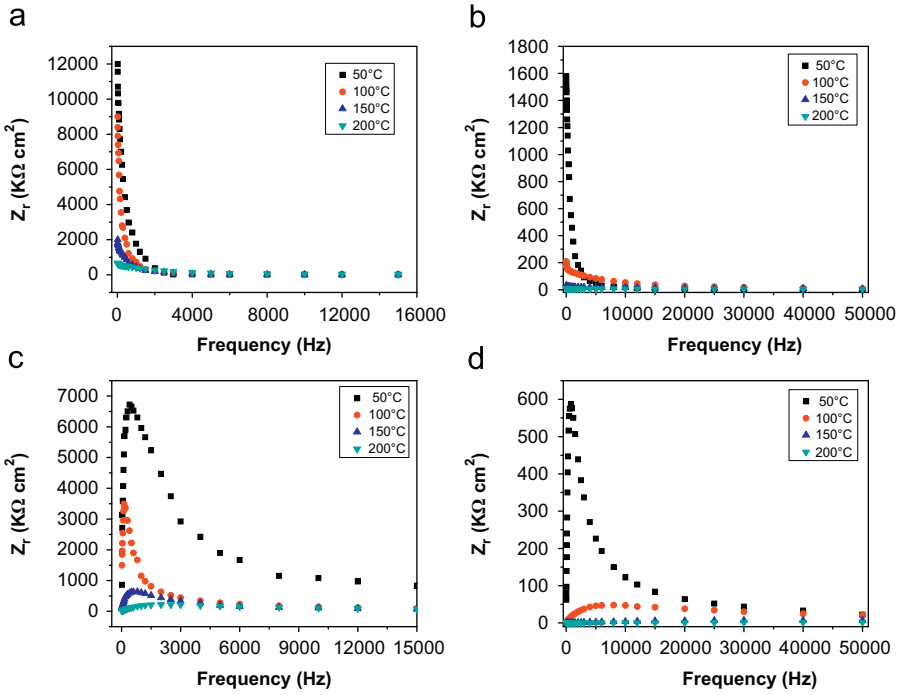

Fig. 8. (a,b) real component w. r. t. frequency and (c,d) imaginary component w. r. t. frequency for pure and 10 at% Al-added iron oxide samples

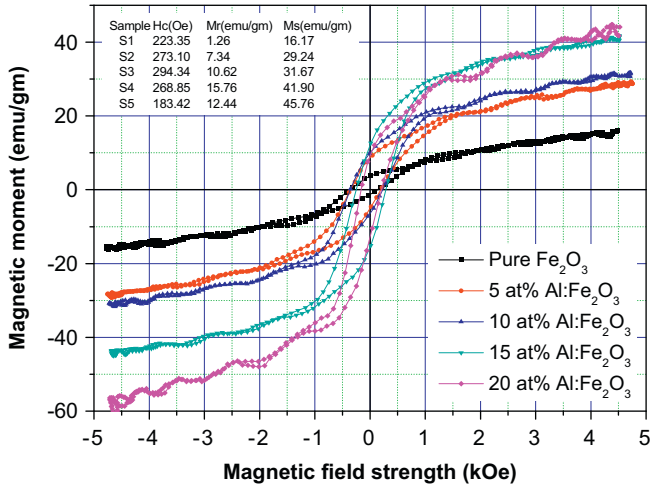

Fig. 9. Magnetic *B*–*H* hysteresis loops of pure and Al-added iron oxide samples.

A-site. The net magnetization, being the difference between A and B sublattice magnetizations, is observed to increase due to the smaller dilution of Fe^{3+} ions at B-site [37]. The incorporation of aluminium ions into the A sublattice leads to decrease in magnetic moment of A sublattice so that the total magnetic moment increases. The remanent ratio $R=M_r/M_s$ is a characteristic parameter of the material. High remanent ratio is desirable for magnetic recording and memory devices. It is an indication of the ease with which the direction of magnetization reorients to nearest easy axis magnetization direction after the magnetic field is removed. The lower value of remanent ratio is indication of isotropic nature of pure iron oxide sample. It is observed from figure that the values of R are in the range 0.071–0.37 and shows increasing trend with aluminium substitution. It is clearly observed from figure that the coercivity (H_c) increases as Al^{3+} content increases up to 10 at% concentration and then decreases for higher concentrations. Low coercivity shows samples are porous in nature, so it requires high field to push the domain wall. The coercivity (H_c) increases rapidly with Al^{3+} content up to 10 at%, but above 10 at% a small change in value has been observed. This may be attributed to unquenched orbital angular momentum of Al^{3+} and to a large anisotropy value [38,39].

4. Conclusions

We have efficiently prepared the pure and aluminium added polycrystalline hematite α-Fe_2O_3 samples by combustion route. The influence of aluminium doping on to the structural, compositional, luminescent and thermal properties of iron oxide samples considering the environment friendliness have been investigated. The existance of interstitial oxygen and its deficiency at higher doping concentration, inductive of declining stoichiometry, whereas more O^{2-} ions locate at the intrinsical sites at low doping concentration is observed. The Fe 2*p* core level is splitted in to two states due to spin orbit copuling. We observed strong violet emission around 436 nm without any deep-level emission due to radiative defects related to the interface traps existing at the grain boundaries and emitted from the radiative transition between these levels and valence band, indicating that the concentration of defects responsible for the deep-level emissions. The specific heat and thermal conductivity study shows the phonon conduction behavior is dominant in these polycrystalline samples. Impedance analysis confirms the grain boundary contribution to the resistance is dominant in the studied frequency and temperature range. The largest coercivity observed for 10 at% sample is about 294.34 emu/gm.

Acknowledgment

The authors are very much thankful to Defense Research and Development Organization (DRDO), New Delhi, for the financial support through its Project no. ERIP/ER/0503504/M/01/007".

References

[1] F. Caruso, Adv. Mater. 13 (2001) 11.
[2] K. Raj, B. Moskowitz, R. Casciari, J. Magn. Magn. Mater. 149 (1995) 174.
[3] R.D. McMichael, R.D. Shull, L.J. Swartzendruber, L.H. Bennett, J. Magn. Magn. Mater. 111 (1992) 29.
[4] P. Tartaj, M.P. Morales, S. Veintemillas-Verdaguer, T. Gonźalez-Carrĕno, C.J. Serna, J. Phys. D: Appl. Phys. 36 (2003) R182.
[5] J.H. Lee, Nat. Med. 13 (2007) 95.
[6] T. Neuberger, B. Schopf, H. Hofmann, M. Hofmann, B. Rechenberg, J. Magn. Magn. Mater. 293 (2005) 483.
[7] C. Connolly, Sensor Rev. 28 (2008) 18.
[8] A. Petri-Fink, M. Chastellain, L. Juillerat-Jeanneret, A. Ferrari, H. Hofmann, Biomaterials 26 (2005) 2685.
[9] M. Khoudiakov, M.C. Gupta, S. Deevi, Nanotechnology 15 (2004) 987.
[10] J. Bao, W. Chen, T. Lui, Y. Zhu, P. Jin, L. Wang, J. Liu, Y. Wei, Y. Li, ACS Nano 1 (2007) 293.
[11] Y.W. Jun, J. Am. Chem. Soc. 127 (2005) 5732.
[12] B. Ravel, E.E. Carpenter, V.G. Harris, J. Appl. Phys. 91 (2002) 8195.
[13] L. Zhang, Y.H. Dou, H.C. Gu, J. Colloid Interface Sci. 297 (2006) 660.
[14] S. Uchida, T. Aida, Nippon Kinzoku Gakkaishi 25 (1961) 276.
[15] A.N. Banerjee, R. Maity, P.K. Ghosh, K.K. Chattopadhyay, Thin Solid Films 474 (2005) 261.
[16] M. Hasegawa, I. Inagawa, M. Tanaka, I. Shirotani, H. Takei, Solid State Commun. 121 (2002) 203.
[17] A.N. Banerjee, K.K. Chattopadhyay, Appl. Surf. Sci. 225 (2004) 243.
[18] X.G. Zheng, K. Taniguchi, A. Takahashi, Y. Liu, C.N. Xu, Appl. Phys. Lett. 85 (2004) 1728.
[19] N. Koriche, A. Bouguelia, A. Aider, M. Trari, Int. J. Hydrogen Energy 30 (2005) 693.
[20] H. Kizaki, K. Sato, A. Yanase, H. Katayama-Yoshida, Physica B 376/377 (2006) 812.
[21] K.P. Ong, K. Bai, P. Blaha, P. Wu, Chem. Mater. 19 (2007) 634.
[22] S. Omeiri, Y. Gabes, A. Bouguelia, M. Trari, J. Electroanal. Chem. 614 (2008) 31.
[23] S.S. Shinde, P.S. Shinde, C.H. Bhosale, K.Y. Rajpure, J. Phys. D: Appl. Phys. 41 (2008) 105109.
[24] S.S. Shinde, P.S. Shinde, S.M. Pawar, A.V. Moholkar, C.H. Bhosale, K.Y. Rajpure, Solid State Sci. 10 (2008) 1209.
[25] Z. Gong, Z.C. Niu, Z.D. Fang, Z.H. Miao, S.L. Feng, Appl. Phys. Lett. 86 (2005) 013104.
[26] J. Baltrusaitis, D.M. Cwiertny, V.H. Grassian, Phys. Chem. Chem. Phys. 9 (2007) 5542.
[27] Y. Li, R.A. van Santen, Th. Weber, J. Solid State Chem. 181 (2008) 3151.
[28] Y. Wang, J. Ma, F. Ji, X. Yu, H. Ma, J. Lumin. 114 (2005) 71.
[29] B.J. Coppa, C.C. Fulton, P.J. Hartlieb, J. Appl. Phys. 95 (2004) 5856.
[30] S.H. Jeong, J.H. Boo, Thin Solid Films 447 (2004) 105.
[31] G.E. Youngblood, R.W. Rice, R.P. Ingel, J. Am. Ceram. Soc. 71 (1988) 255.
[32] J.P. Suchet, Chimie physique des semi-conducteurs, Paris:Dunod, 1962. Translated under the title Fizicheskaya khimiya poliprovodnikov, Moscow: Metallurgiya, 1969.
[33] T.G. Xi, Thermo-physical Properties of Inorganic Materials, Shanghai Scientific and Technical Press, Shanghai, 1981.
[34] P.G. Klemens, Physica B 263 (1999) 102.
[35] D.K. Pradhan, B.K. Samantary, R.N.P. Chaudhary, A.K. Thakur, Mater. Sci. Eng. B 116 (2005) 7.
[36] J. Wang, F.Q. Wu, G. Song, N. Wu, J.P. Wang, Ferroelectrics 323 (2005) 71.
[37] J. Smit, H.P.J. Wijn, Ferrites, Cleaver-Human Press, London, 1959.
[38] S.M. Patange, S.E. Shirsath, B.G Toksha, S.S Jadhav, K.M Jadhav, J. Appl. Phys. 106 (2009) 023914.
[39] H. Wang, Y. Li, L. Sun, Y. Li, W. Wang, S. Wang, S. Xu, Q. Yang, J. Coll. Interface Sci. 350 (2010) 396.